Front. Struct. Civ. Eng. 2024, 18(12): 1845–1864
https://doi.org/10.1007/s11709-024-1123-x

RESEARCH ARTICLE

Mechanical properties of segment joints in subway shield tunnels by a full-scale test

Pengfei LI[a], **Wu FENG**[a], **Xiaojing GAO**[a*], **Ziqi JIA**[a], **Haifeng WANG**[b], **Zenghui LIU**[b]

[a] *Key Laboratory of Urban Security and Disaster Engineering, Ministry of Education, Beijing University of Technology, Beijing 100124, China*
[b] *Nantong Railway Construction Component Co., Ltd., Nantong 226000, China*
[*]*Corresponding author. E-mail: gxj050195@163.com*

ABSTRACT In this article, the mechanical properties of tunnel joints with curved bolts are studied and analyzed using the research methods of full-scale testing and finite element numerical simulation. First, the experiment results were analyzed to find out the development law of stress and strain of concrete in each part of the tunnel fragment when bearing. The damage process of the joint of the tunnel fragment was described in stages, and the characteristic load value that can reflect the initial bearing capacity in each stage was proposed. Afterward, using the ABAQUS three-dimensional (3D) finite element numerical modeling software, a numerical model corresponding to the experiment was established. The mid-span deflection was used to observe the change in loading and the destruction of each stage, comparing it to the proposed form to verify the reasonableness of the numerical model. Finally, the numerical models were used to analyze the change in material parameters and external loads from two aspects. It is concluded that the damage process of tunnel joints under curved bolt connection can be divided into concrete elasticity stage, inner arc cracking stage, overall joint damage stage, and ultimate joint damage stage, and the initial load of the adjacent stages is defined as the characteristic load value. After concrete cracking occurs, the bolts start to become the main load-bearing components, and the bolt stress grows rapidly in stage II. The strain development of the concrete on the outer arc is greater than the strain value of the concrete on the side due to mutual contact and extrusion. The parameters were changed for material properties, and it was found that increasing the concrete strength and bolt strength could improve the shield fragment joint bearing performance. The optimal effect of improving the mechanical properties of the shield fragment joint would be obtained when the concrete strength grade is C60, and the bolt strength grade is 8.8. Increasing the size of the axial force and bolt preload has the most obvious effect on the load-carrying capacity in the initial elastic phase. This can reduce the joint angle and thus improve joint stiffness. Meanwhile, increasing the axial force has a greater effect on the performance of the tunnel joint than the bolt preload.

KEYWORDS shield tunnel, failure mechanism, bearing capacity, segment joint

1 Introduction

With the continuous development of underground space, the shield method is widely used in urban underground transportation construction because of its advantages of fast, safe, and environmental protection construction [1–4]. Shield lining consisting of reinforced concrete (RC) precast pipe pieces and bolts [5–7]. The joint is the weakest part of the force [8–12], and the mechanical properties of the joints directly determine the load-bearing capacity and safety performance of the tunnel structure [13–17]. Therefore, it is necessary to research the load-bearing performance and damage mechanism of shield tunnel segment joints.

In the segment joints test, Zhang et al. [18] studied the mechanical damage characteristics of segment joints by full-scale tests, divided the whole damage process of joints into small deformation, large deformation, stable bearing, and damage stages, and summarized the crack expansion process. Zuo et al. [19] studied the mechanical

Article history: Received Oct 18, 2023; Accepted Apr 5, 2024

behavior of segment joints under compression bending by prototype loading tests, analyzed the relationship between the joint opening and the internal force of the joint, and summarized the mechanical characteristics of the joint bolts and the development law of cracks at the tube sheet joints. Wang et al. [20] analyzed the deformation characteristics and mechanical characteristics of the pipe sheet joints using full-scale indoor tests and numerical simulation studies, analyzed the bolts' damage characteristics, the cracks' development process at the joints, and the stress change law at the pipe sheet joints. Liu et al. [21] studied the mechanical behavior of single-ring and multi-ring tube sheet joints by full-scale tests, clarified the joint failure characteristics and damage mechanisms, summarized the load and deformation change laws at single-ring and multi-ring tube sheet joints, and found that the bending moment, longitudinal and radial displacement at the longitudinal joint of multi-ring tube sheet was smaller. Still, the crack width was wider than the single-ring tube sheet at the joint site. Wang et al. [22] studied the damage performance of pipe sheet joints with straight bolt connections by full-scale pull-out tests. They summarized the load-bearing mode and damage mechanism of ring joints with straight bolt connections by analyzing the failure characteristics of the joints under different load conditions and the development process of cracks in the hand hole area. Zhang et al. [23] used full-scale tests on pipe sheet joints to study the variation laws of joint tension, turning angle, joint deflection, and concrete strain. They summarized the force-deformation characteristics of the joints. Liu et al. [24] and Shi et al. [25] studied the deformation characteristics of tube joints under unloading conditions, the effect of lateral unloading on tube joints during lateral excavation of existing shield tunnels, and established corresponding deformation control standards based on the overall deformation indexes of tunnels, and also came to the conclusions that displacement during tunnel unloading leads to a sharp increase in the stresses at the joints of the tubes, cracks in the concrete at the joints, an increase in the stresses in joint bolts, and a decrease in the overall waterproofing performance.In addition, numerical simulation is widely used to study the mechanical properties of segment joints. Chen et al. [26] used numerical simulations and engineering examples to compare and analyze. They concluded that the lining bulging in the soft soil shield tunneling process includes three stages of misalignment, tension, and stable deformation, which will inevitably lead to an increase in the force at the lining joints. At the same time, the longitudinal bolts will also generate stress concentrations due to misalignment. Karami et al. [27] carried out a study on the performance change of composite castellated steel beam (CCSB) under fire and summarized the change rule of the influence of each parameter on the performance of CCSB by varying the parameters analytically based on a nonlinear finite element numerical model with slab concrete thickness, beam length, castellated beam section, and temperature separately as variables. Shishegaran et al. [28] conducted a study on enhancing the flexural capacity of RC frames through a combination of experiments and finite element numerical simulations. The validity of the model is evaluated by analyzing the load-deflection results by finite element and validating them with the experiment. The transferred stress system (TSS) fixed beams were found to improve the load carrying capacity of the structure and a recommendation to use TSS fixed beams instead of normal RC beams in RC frames was derived. Shishegaran et al. [29] analyzed the mechanical properties of reinforced concrete panels (RCP) by means of nonlinear finite elements and surrogate models, and the resistance under blast loading was investigated by varying the parametric analysis. The optimal model of RCP under each parameter value is summarized, and the change rule of the influence of each parameter on RCP is explored. Bigdeli et al. [30] investigated and analyzed reinforced concrete tunnel in internal water pressure conditions using nonlinear finite element with variable parameter analysis for the compressive and tensile strength of concrete, the size of the longitudinal reinforcement bar, the transverse bar diameter, and the internal water pressure. The study of the variation rule of its influence on the mechanical properties of the structure concluded that the mechanical properties of the concrete material as well as the internal water pressure have the greatest influence on the RCT. Zhao et al. [31] used numerical simulation to study the pipe segments' mechanical properties in the underwater excavation surface surge and clarify the mechanical change law of concrete strain and bolts at the joints. Tsiampousi et al. [32] used physical tests combined with numerical simulations to study the joint bolts, determined the effect of positive and negative bending moments on the bearing performance of the bolts by changing the loading direction, and elucidated the effect of the joint bolts on the stiffness of the joint. Shishegaran et al. [33] studied and analyzed the reinforced concrete connections (RCC) parameters under post-earthquake fire conditions by finite element simulation including the parameters of beam depth, compressive strength of the concrete, percentages of beam and column longitudinal reinforcements. It is found that the parameter that contributes the most to RCC enhancement is ratio of longitudinal bars of column and it helps more to enhance the performance of RCC as compared to ratio of longitudinal bars of beam. Meanwhile, increasing the compressive strength of concrete enhances the load carrying capacity of RCC under post-earthquake fire conditions and the higher the temperature, the more significant the enhancement effect is. Finally, a reliable factor of safety for the use of RCC is summarized. Naghsh et al. [34] used nonlinear finite element numerical simulation to study column-tree moment connection (CTMC) under fire and static loads with parametric analysis of applied temperature, number of flange bolts, number of web bolts, length of the beam, and applied static loads. It was finally concluded that the change in deflection of the CTMC depends mainly on the temperature, while the length of the beams affects the fire resistance, which increases as the length of the structural beams decreases, and thus, shorter beams increase the overall fire resistance of the structure. Kou et al. [35] used numerical simulation to study the flexural stiffness of large-diameter shield pipe segment joints under high water pressure and different axial loads. They analyzed the concrete strength on the bearing capacity of the joint. The enhancement of the flexural stiffness of the joint is related to the strength of the connection bolts, summarizing the damage characteristics of the joint and the crack formation process.

In terms of theoretical analysis, Dong et al. [36] used experiments and theoretical calculations to investigate the mechanical behavior of pipe fragment joints. By analyzing the effect of external load on joint stiffness, they summarized the variation law of joint stiffness and internal force. They analyzed the factors affecting the internal pressure of the joint and their influence on the law. Li et al. [37] established a theoretical, analytical model of the pipe segment joint, analyzed the stress and deformation characteristics of the joint under the action of hydrostatic pressure, summarized the law of change of joint tension with water pressure, and obtained the stress concentration area and stress change law of the joint bolt through bolt shear test. Zheng et al. [38] established a tunnel safety assessment system with the damage characteristics of tube segments and bolts for the tunnel collapse damage mechanism.

Nonetheless, the majority of prior research focuses on how the segment's load affects bearing properties and the process of damage, with a notable absence of studies and analyses regarding the segment joint's impact on bearing efficiency and damage traits. This study methodically examines the bending damage traits of the segment joint, focusing on material characteristics and external structural loads, through comprehensive tests and three-dimensional (3D) numerical simulations. A summary was provided of how factors such as concrete and bolt strength, axial force, and prestressing of bolts affect joint bearing efficiency, aiding in joint design and safety evaluations. The flowchart of the article research is shown in Fig. 1.

2 Full-scale test

2.1 Test overview

For conducting a comprehensive test, a section of the city metro shield was chosen, featuring a shield tunnel with an external diameter of 6200 mm and an internal diameter of 5500 mm. Every liner ring is composed of six parts, featuring a capping segment at a 20° circular center angle, two neighboring segments at a 68.75° circular center angle, and three traditional segments at a 67.5° circular center angle. This segment measures 350 mm in thickness, 1200 mm in width, and is linked to the circumferential joint by a pair of M30 bending bolts, each with a strength grade of 8.8. For this examination, the

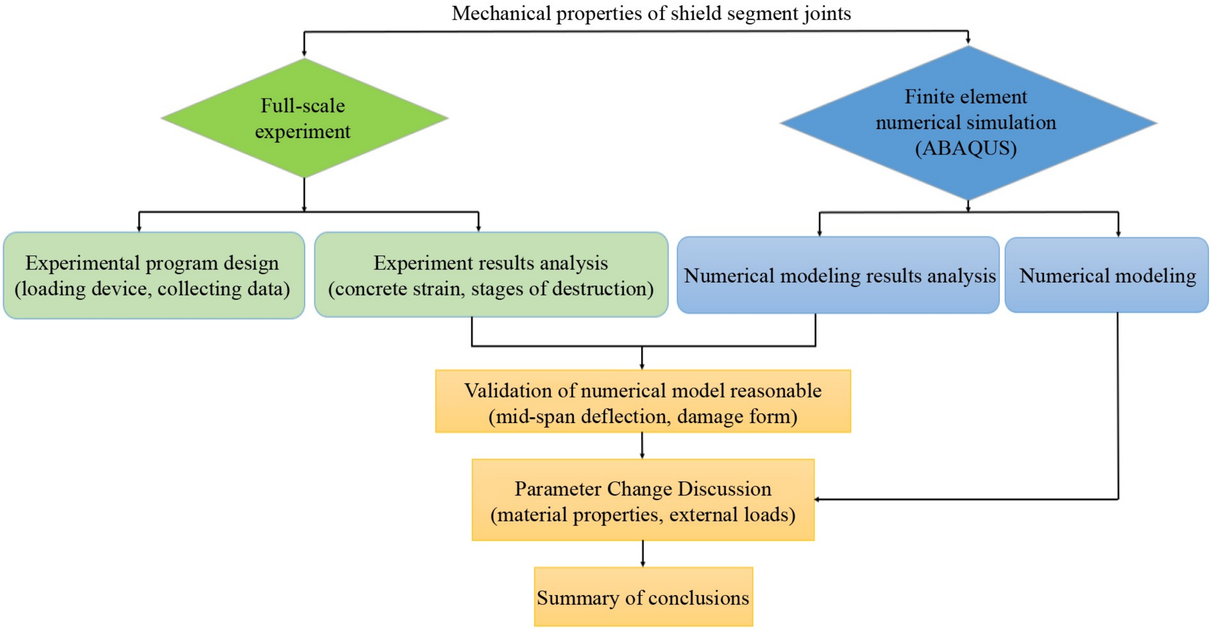

Fig. 1 Research flowchart.

conventional block is chosen, with the joint’s configuration depicted in Fig. 2.

As depicted in Fig. 3, the testing load system is composed of a reaction frame, load beam, loading plate, hydraulic jack, and a horizontal sliding support. The vertical force of the hydraulic jack is uniformly distributed across the component through a load distribution beam and a cushion. The load cushion can effectively avoid stress concentration caused by the small contact area between the load distribution beam and the tube sheet. The test loading method for graded loading involves applying 10 kN at each level of loading. When the lower part of the bolted concrete is about to fall off, it is determined that the segment has lost its bearing properties, and loading is immediately stopped.

The content of the test monitoring mainly includes deflection at the joint, joint tension, horizontal displacement of the segment, concrete strain, and crack width. To reflect the damage characteristics of the segments, concrete strain monitoring points are arranged symmetrically on the inner and outer arcs of the segments and on the sides. Two displacement sensors are symmetrically placed on the tube sheet's inner arch and end face to monitor the joint tension during joint damage. The specific monitoring point arrangement is shown in Fig. 4.

Table 1 shows the range, accuracy, and number of instruments used for the above measurement elements.

2.2 Test results

2.2.1 Joint destruction process

As shown in Fig. 5, the load−deflection variation curve exhibits prominent segmentation characteristics, and the joint damage process can be divided into four stages according to the variation pattern. The M1 measurement point, which is closer to the joint, can better illustrate the damage process and characteristics of the joint, so the load−deflection curve of M1 is mainly used to determine the mechanical properties of each damage stage.

Stage I (Concrete elastic stage). By securing the bolts prior to loading, preload is generated, and the initial load is minimal, ensuring that the two parts are tightly packed in the center and resist bending. As the load escalates, there’s a steady rise in the angle at which the inner arc joint opens, accompanied by a minor linear increase in deflection. Compared to the M1 measurement point, the G1 measurement point lies at a greater distance from the joint. At this point, the bending pattern is more gradual, the stretchable phase endures for an extended period, and the tube sheet’s surface lacks noticeable fissures. To summarize, this stage is characterized by the tangible elastic phase. As shown in Fig. 6, the force on the bolt is almost zero.

Stage II (Inner arc cracking stage). The M1 measurement point is closer to the joint, so concrete cracking has an earlier and more severe effect on the deflection of this measurement point. When the external load reached 64 kN, the hand hole at the inner curved surface concrete cracked, as shown in Fig. 7(a). At this time, the concrete near the G1 measurement point did not show cracking, but also in the elastic stage. As the load increases, cracks develop along the width direction of the

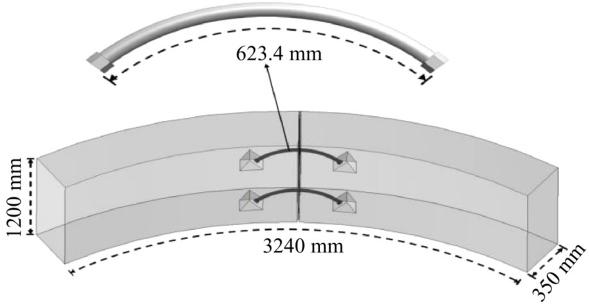

Fig. 2 Segment joint.

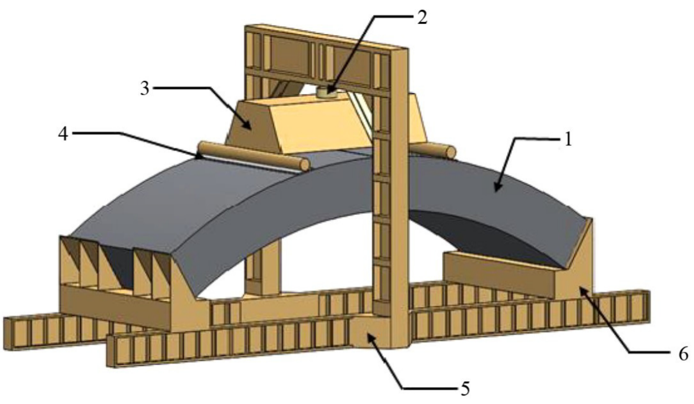

1: Test specimen 2: Load actuator 3: Load-distribution girder
4: Load cushion 5: Reaction frame 6: Horizontal sliding bottom support

Fig. 3 Test loading system.

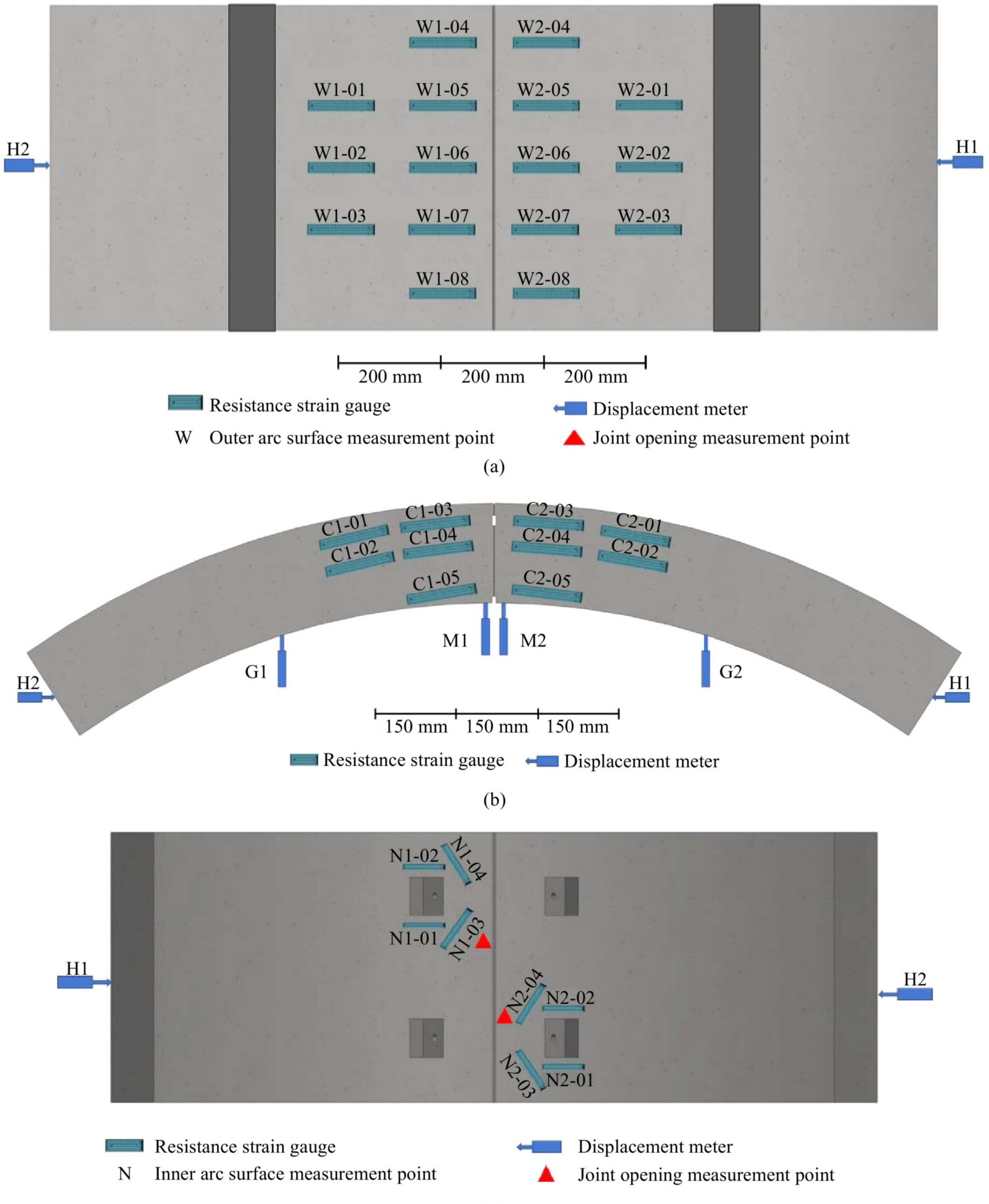

Fig. 4 Diagram of monitoring points: (a) outer arc monitoring point; (b) side monitoring points; (c) internal arc monitoring point (H, M, and G represent horizontal displacement meter, near joint displacement meter, and far joint displacement meter, respectively; C represents the strain gauge position (on the side)).

Table 1 Test instruments

Measurement content	Instrument	Range	Accuracy	Quantity
Joint deflection	displacement monitor	100 mm	0.1 mm	2
Load plate deflection	displacement monitor	100 mm	0.1 mm	2
Concrete strain	strain gauges	1500×10^{-6}	0.5×10^{-6}	34
Crack width	crack monitor	20 mm	0.01 mm	1
Joint opening	displacement monitor	20 mm	0.1 mm	4

segment, marking the segment's entry into the internal arc damage stage, defining the initial load of this stage as the cracking load (represented by f_t). The deflection at the M1 measurement point increases sharply at this stage, but the deflection value at the G1 measurement point still shows a slight trend due to the development of the crack from the inner arc surface near the hand hole. After the load reaches 76 kN, the lateral concrete cracks (Fig. 7(b)). The crack development direction is consistent with the bent bolt profile because the inner arc surface concrete has cracked, and the outer arc surface concrete is not yet in contact. In contrast, the bolt tension increases sharply, causing the main load-bearing member to shift from the inner arc surface concrete to the bolt. With the load reaching 91 kN, a crack developed near the G1 measurement point, and the deflection of this measurement point began to increase significantly. Although the duration of the two measurement points, M1 and G1, in phase II was different, the overall trend of change coincided with the damage characteristics of the test.

Stage III (Joint overall damage stage). When the external load reaches 128 kN, the crack at the position of the handhole on the inner arc surface runs along the width direction of the tube sheet, as shown in Fig. 8(a), and the concrete on the outer arc surface of the joint is closely packed as shown in Fig. 8(b), so the characteristic loads corresponding to M1 and G1 measurement points when they enter stage III are the same, while the concrete strain at the joint on the outer arc surface increases sharply, and the external load at this time is defined as the damage load (represented by f_c). After the concrete is extruded onto the outer arc surface, the bending resistance of the joint is enhanced, and the rate of deflection growth slows down. Followed by the complete extrusion of concrete on the outer arc surface and the gradual appearance of

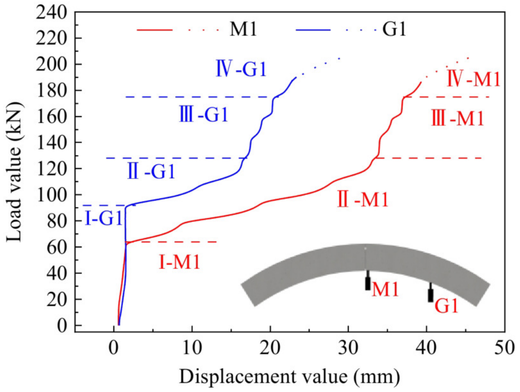

Fig. 5 Load−deflection variation diagram.

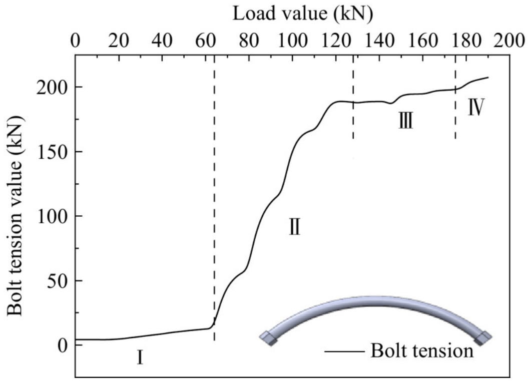

Fig. 6 Bolt tension variation diagram.

(a) (b)

Fig. 7 Inner arc cracking stage damage: (a) inner curved surface hand hole cracking; (b) side concrete cracking.

(a) (b)

Fig. 8 Overall damage of the joint: (a) hand hole for curved inner surface; (b) outer curved surface contact.

cracks, the growth of tension of the bolts slows down, marking the transformation of the primary load-bearing member from bolts to concrete on the outer arc surface.

Stage IV (Joint limit damage stage). The load reaches 174 kN, the concrete on the outer arc surface begins to crush, and the lateral concrete runs along the direction of the bolt profile to the inner arc surface and connects with the crack that extends at the location of the hand hole on the inner arc surface, as shown in Figs. 9(a) and 9(b). The concrete on the outer arc surface gradually detached from the structure, and the bolt tension slightly increased compared to stage III. Due to the small value of the axial force applied in the test, the bolt did not yield during the loading process. The load increased to 190 kN, and the outer arc surface joints of the concrete experienced extensive crushing and peeling. Meanwhile, on the inner arc surface handhole, a blockage phenomenon occurred on the side of the concrete under tension, rendering it unable to continue supporting the load. The final damage is determined by the crushing off of concrete on the side and outer arc surfaces, as shown in Figs. 8(c) and 8(d), and the initial load at this stage is defined as the ultimate load (represented by f_u). The dashed line in Fig. 5 shows the trend of deflection with load at the end of the test loading.

2.2.2 Concrete strains

1) Concrete strain on the outer arc

Select three positions, W1-05, W1-06, and W1-07, and plot the strain versus load variation curve as shown in Fig. 10(a). The concrete is specified to have a negative compressive stress and a positive tensile strain. According to the law of change, each stress–load curve can be divided into four damage stages. The vertical load is less than 64 kN, and the tension angle of the lower part of the joint is slight, so the concrete strain at the location of the three measurement points is almost 0. As the load increases, the lower part of the joint tension increases, leading to the upward movement of the concrete pressure zone of the joint, and the upper half generates compressive strain. The vertical load reaches 128 kN, the concrete on the outer curved surface is dense, and the line variation increases sharply. After the load reaches 175 kN, as the concrete on the outer arc of the joint starts to crush, the trend of curve change slows down until the end of the load, while the W1-06 measurement point is in the middle of the bolt, there is a stress superposition phenomenon, so W1-06 as a whole is more significant than W1-05 and W1-07.

The strain–load relationships at the two positions, W1-01 and W1-02, are shown in Fig. 10(b), and their trends are also consistent with the four damage stages. In stage I, the strains at W1-01 and W1-02 are less than zero because the two measurement points are within the influence of the loaded beam load. Because the measurement point is close to the load buffer pad in stages II and III, stress concentration will result in compressive strain when applied, so the curve keeps

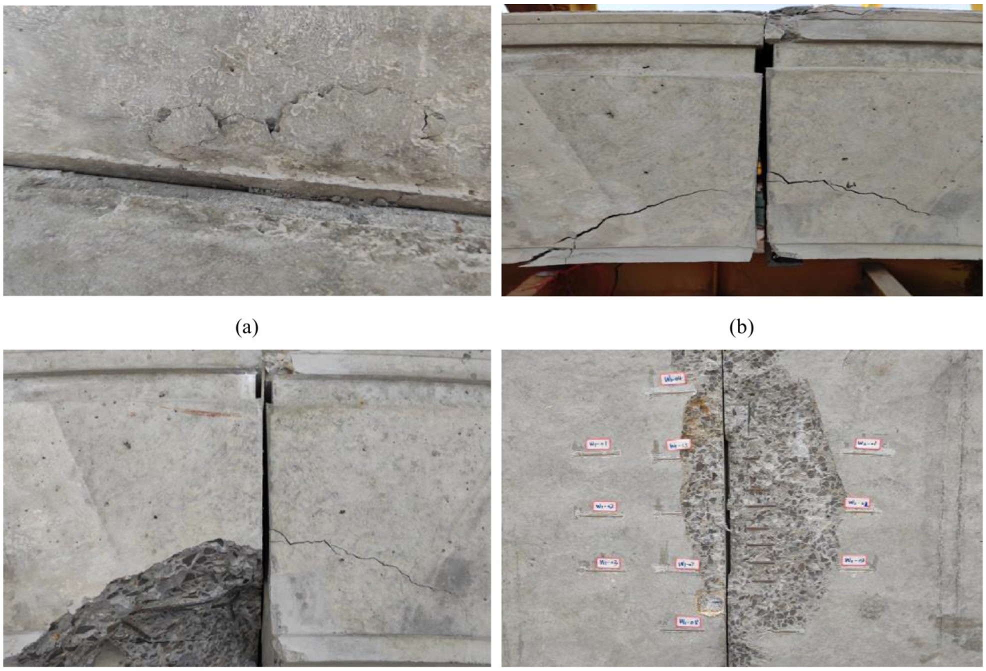

Fig. 9 Terminal failure state of the joint: (a) the outer arc concrete is crushed; (b) side penetration cracks; (c) side concrete peeling; (d) concrete peeling from the outer arc.

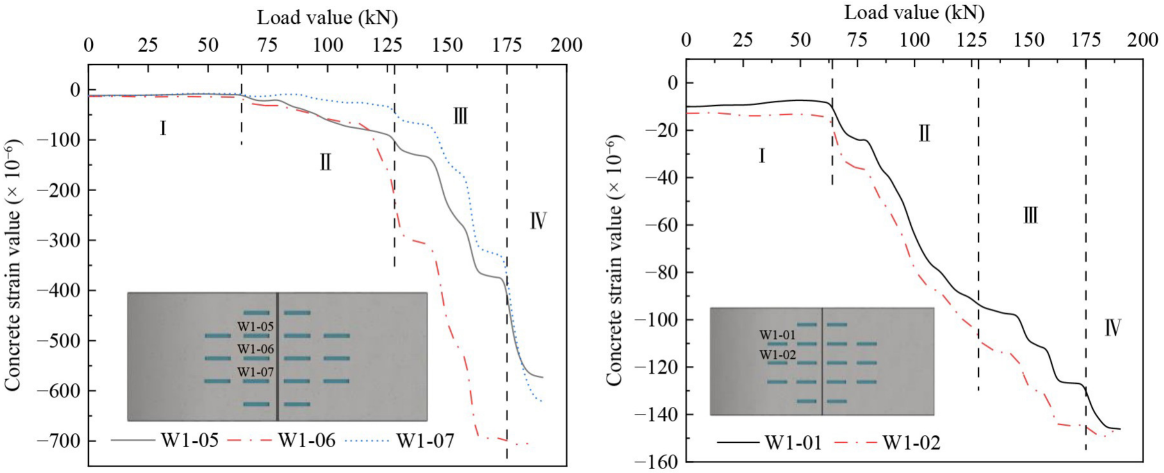

(a) (b)

Fig. 10 Outer arc surface strain–load variation diagram: (a) near joint monitoring point; (b) remote joint monitoring point.

growing faster. In stage IV, the line growth rate decreases compared to stage III.

2) Concrete strain in inner arc hand hole

In the test, the bolt tension cracked the concrete at the inner arc's hand hole earlier. When the crack width is too large, the strain gauges at this location are pulled off, and the subsequent strain data cannot be collected. Therefore, the strains at the inner arc of this subsection are all data from before cracking occurred at the location. As shown in Fig. 11. The concrete at positions N1-02 and N1-03 is subjected to tension throughout under the action of the bolts. Since the crack at the hand hole develops in the 45° direction of the hand hole angle, N1-03 is located in the main development direction of the crack. Hence, the stress change in the concrete at this position is more pronounced, and its tensile strain is much higher than that of N1-02.

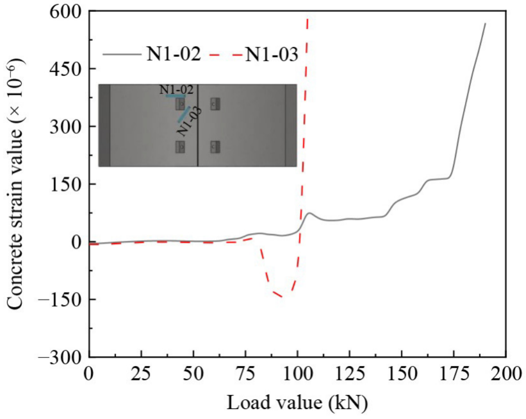

Fig. 11 Strain–load variation diagram.

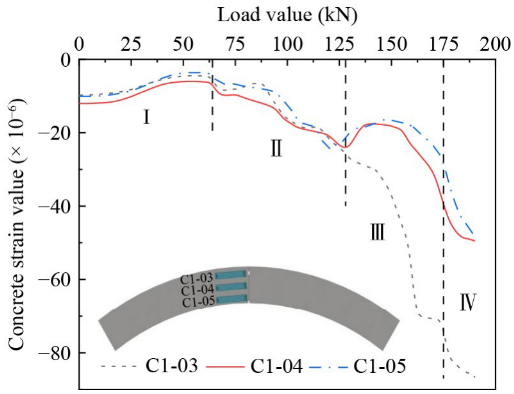

Fig. 12 Side strain–load variation diagram.

3) Side concrete strain

The load strain at the three measurement points, C1-03, C1-04, and C1-05, is shown in Fig. 12. Due to the initial bolt preload in stage I, the strain at all three measurement points is less than 0. In stage II, the concrete compressive strain increases with the load. Still, the fluctuation of the upward shift of the compressive strain curve occurs in this stage because the lower part of the joint is gradually opening, and the concrete pressure zone at the joint is shifting upward. After entering stage III, the concrete contact on the outer arc surface improves the force performance, the C1-03 curve increases, and the compressive strain value at the end of this stage is much higher than C1-04 and C1-05. In addition, although cracks have occurred in the concrete on the arc surface along the width of the tube segment in the direction of penetration, cracks also appeared on the side because the concrete's compressive capacity is much greater than its tensile capacity. The concrete in the middle part of the joint is still in contact with pressure, so C1-04 and C1-05, two lines in the compressive strain stage, appeared to decrease and then increase, showing an obvious upward trend. In stage IV, the concrete on the outer arc is crushed, and the growth trend of the C1-03 curve decreases compared with stage III, while the tension of the lower part of the joint increases, and the rise of strain value at C1-04 and C1-05 gradually decreases. Furthermore, during stage III, the strain value of concrete at C1-03 escalates more rapidly than at the other two measurement points due to the external arc surface's concrete touching and being compressed, leading to damage on the outer arc's concrete and a corresponding reduction in strain value in line with the load variation trend.

2.2.3 Joint stiffness

Figure 13 represents the relationship between the variation of the bending moment of the tunnel segment joints and the angle of the shield segment joints in the experiment, with the vertical coordinate indicating the value of the bending moment and the horizontal coordinate indicating the value of the angle. According to the changing law of this graph, it can be divided into four stages of development, corresponding to the stage of experimental destruction. At the initial stage, the increase in tunnel joint angle with bending moment is not significant, which is due to the small initial load applied and the presence of friction between the fragments. At stage II, with the increasing load, the shield fragments cracked, and the rate of change of the joint angle of the shield fragments with the bending moment accelerated. After entering stage III, the concrete contact on the outer curved surface improves the flexural properties of the joint, so that the curve abruptly changes when M = 195 kN·m, and the growth of the joint opening angle slows down. When the bending moment increases to 267 kN·m in stage IV, the growth rate of the joint opening angle decreases compared to stage III. At a bending moment of 291 kN·m, there was a large area of damage to the concrete on the outer arc and sides, and most of the crack failure damage occurred on the inner arc.

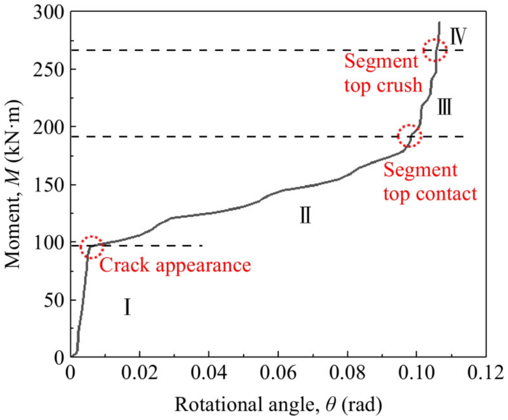

Fig. 13 Rotaional angle (θ)–moment (M) diagram.

3 Numerical simulation analysis

3.1 Numerical model

Through the full-scale loading test on the shields segment joints, the development of concrete strain and the damage stage were analyzed. In this section, a 3D numerical model corresponding to the experiment is established by the numerical software of ABAQUS, as shown in Fig. 14. The concrete grade in the model is C50, and the strength grade of the bolts is 8.8. In the numerical simulation process, the loading plate deformation is not considered, and it is regarded as a rigid body with tie constraint contact type with the outer arc of the shield segment. Meanwhile, as shown in Fig. 15, the shield segment concrete was used as Surface-to-Surface contact type with attributes Tangential Behavior —Penalty with a value of 0.6 and Normal Behavior—“Hard” contact. The concrete and the bolts used Surface-to-Surface contact type, Tangential Behavior—Penalty with a value of 0.3 and Normal Behavior—“Hard” contact. The nuts and bolts are of tie constraint contact type. In addition, the boundary conditions of the model were set to allow displacement along the X-direction at one end, limiting displacement in the remaining directions, and an articulated support at the other end, limiting model displacement in the Z-axis direction as shown in Fig. 16.

In the process of numerical model meshing, in order to obtain a higher quality amount of grid cells and improve the calculation accuracy, the grid was first partitioned and

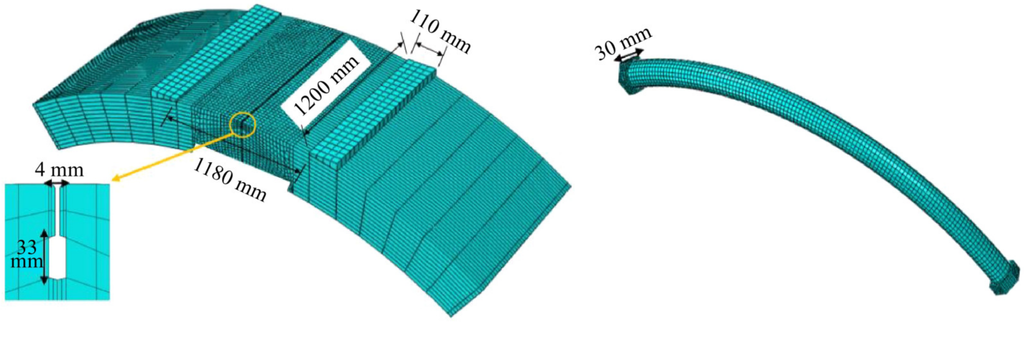

(a)

(b)

Fig. 14 Finite element model diagram: (a) segment model; (b) bolt model.

divided, and the area was meshed sequentially one by one. The shield segment meshes were all meshed using a hexahedral swept-neutral axis algorithm with minimized mesh transitions. The number of local seed cells is set to 12 for the bolt hole part. The number of local seed cells is set to 8 and 10 according to the length of the peripheral curved surface of the model, and the bolts, nuts, and load plates are divided by using hexahedral structural attributes. All the cell types are in the Standard-3Dstress-C3D8R cell model. After that, shape checking, size checking and analysis checking of the delineated mesh were carried out, and there were no erroneous cells, and the ratio of warning cells to all cells was 3.65%, which was in line with the requirements of the model calculation.

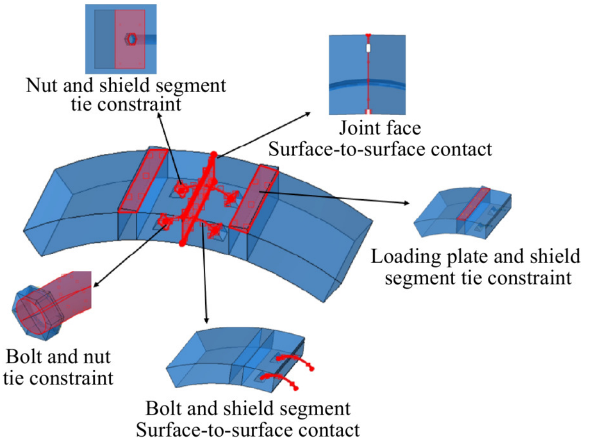

Fig. 15 Contact diagram of model parts.

3.2 Intrinsic model and parameters

The concrete in the finite element model uses the plastic damage principal structure model [39,40], and the strength grade of concrete is C50. According to the concrete principal structure relationship in the Code for the Design of Concrete Structures GB50010-2010, the stress–strain relationship model for concrete uniaxially stressed [41] and tensioned is obtained, as shown in Fig. 17.

The expressions of the uniaxial compressive stress–strain relationship model for concrete are as follows:

$$\sigma_c = (1 - d_c) E_c \varepsilon_c, \tag{1}$$

$$d_c = \begin{cases} 1 - \dfrac{\rho_c n}{n - 1 + x_c^n}, & x_c \leqslant 1 \\ 1 - \dfrac{\rho_c}{\alpha_c (x_c - 1)^2 + x_c^n}, & x_c > 1 \end{cases} \tag{2}$$

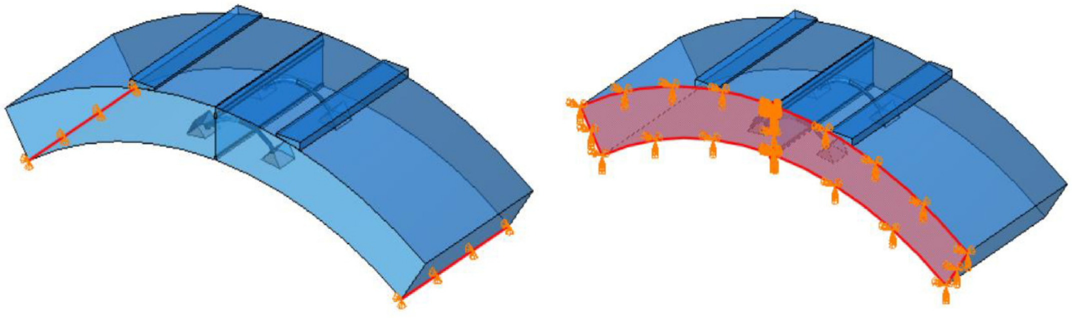

(a) (b)

Fig. 16 Model constraint diagram: (a) *X*-direction constraint; (b) side constraints.

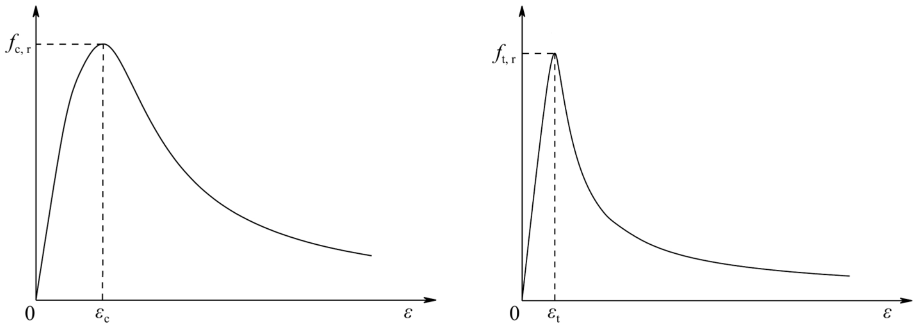

(a) (b)

Fig. 17 Concrete stress–strain diagram: (a) uniaxial compressive stress–strain diagram of concrete; (b) uniaxial stress–strain diagram of concrete under tension.

$$\rho_{\mathrm{c}} = \frac{f_{\mathrm{c,r}}}{E_{\mathrm{c}}\varepsilon_{\mathrm{c,r}}},\ x_{\mathrm{c}} = \frac{\varepsilon_{\mathrm{c}}}{\varepsilon_{\mathrm{c,r}}},$$

$$n = \frac{E_{\mathrm{c}}\varepsilon_{\mathrm{c,r}}}{E_{\mathrm{c}}\varepsilon_{\mathrm{c,r}} - f_{\mathrm{c,r}}}, \tag{3}$$

where α_{c} represents the value of the falling section of the uniaxial compressive stress–strain line in concrete; $f_{\mathrm{c,r}}$ represents the uniaxial ultimate compressive strength of concrete, taking the value of 32.4 MPa; $\varepsilon_{\mathrm{c,r}}$ represents the peak compressive strain of concrete corresponding to the uniaxial maximum compressive strength, takes the value of 0.00168; d_{c} represents the uniaxial compressive damage evolution parameters of concrete; E_{c} represents the modulus of elasticity of concrete.

The expressions of the uniaxial stress–strain relationship model for concrete in tension are as follows:

$$\sigma_{\mathrm{t}} = (1-d_{\mathrm{t}})E_{\mathrm{c}}\varepsilon_{\mathrm{t}}, \tag{4}$$

$$d_{\mathrm{c}} = \begin{cases} 1-\rho_{\mathrm{t}}[1.2-0.2x_{\mathrm{t}}^{5}], & x_{\mathrm{t}} \leqslant 1 \\ 1-\dfrac{\rho_{\mathrm{t}}}{\alpha_{\mathrm{t}}(x_{\mathrm{t}}-1)^{1.7}+x_{\mathrm{t}}}, & x_{\mathrm{t}} > 1 \end{cases} \tag{5}$$

$$\rho_{\mathrm{t}} = \frac{f_{\mathrm{t,r}}}{E_{\mathrm{c}}\varepsilon_{\mathrm{t,r}}},\ x_{\mathrm{t}} = \frac{\varepsilon_{\mathrm{t}}}{\varepsilon_{\mathrm{t,r}}}, \tag{6}$$

where α_{t} represents the parameter value of the falling section of the uniaxial stress–strain curve of concrete; $f_{\mathrm{t,r}}$ represents the uniaxial ultimate tensile strength of concrete, taking the value of 2.64 MPa; $\varepsilon_{\mathrm{t,r}}$ represents the peak tensile strain of concrete corresponding to the uniaxial maximum tensile strength and takes the value of 0.000076; d_{t} represents the uniaxial tensile damage evolution parameters of concrete.

The bifold intrinsic structure model is chosen to describe the mechanical behavior of the bolt, as shown in Fig. 18. The bolts are made of No. 45 steel, which has a yield strength of 640 MPa and a modulus of elasticity of 206 GPa.

$$f_{\mathrm{s}} = \begin{cases} E_{\mathrm{s}}\varepsilon_{\mathrm{s}}, & \varepsilon_{\mathrm{s}} \leqslant \varepsilon_{\mathrm{e}} \\ f_{\mathrm{y}}+\eta(\varepsilon_{\mathrm{s}}-\varepsilon_{\mathrm{e}}), & \varepsilon_{\mathrm{e}} < \varepsilon_{\mathrm{s}} \leqslant \varepsilon_{\mathrm{u}} \end{cases} \tag{7}$$

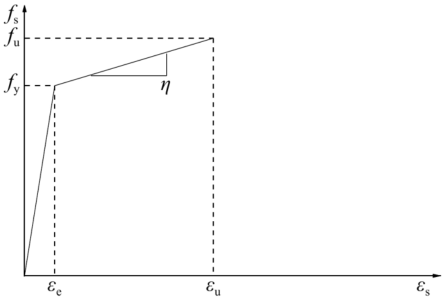

Fig. 18 The bifold intrinsic structure model of the bolt.

where E_{s} is the modulus of elasticity of the bolt material, ε_{e}, ε_{u} represent the yield strain and the peak strain of the bolt, respectively; ε_{s} represents the strain after yielding of the bolt material; f_{y} is the yield strength of the bolt material; f_{u} is the ultimate strength of material; η is the slope of the hardened section of the material with the value $\eta = \dfrac{f_{\mathrm{u}}-f_{\mathrm{y}}}{\varepsilon_{\mathrm{u}}-\varepsilon_{\mathrm{e}}}$.

3.3 Comparison of simulation and test results

3.3.1 Final damage state and process

Figure 19 compares the final damage effects between numerical simulation and testing. From the stress cloud diagram of the numerical model reaching the final damage state, it can be observed that the simulated crack development trend and the concrete breakage are similar to the test. The measurements of plastic strain in both the segment's hand hole region and the lateral concrete reveal that the fracture's ultimate form on the segment's side closely aligns with the bolt's profile, with the crack emerging across the segment's width in the inner arc hand hole zone and spreading to both sides. The observed pattern of damage aligns with the outcomes of the tests. From the preceding analysis, it is evident that the ultimate damage conditions of the test and the computational simulation align closely, clearly showing the numerical model's effective representation of the test's damage traits [42–46].

Simulated and tested joint stiffness, as well as load-displacement changes, are also analyzed. Figure 20 shows the comparison of joint stiffness curves, and Fig. 21 shows the comparison of load deflection. As shown in Fig. 20, the joint angle increases with the bending moment M. The stiffness of joint bending, denoted as $k_{\theta} = \mathrm{d}M/\mathrm{d}\theta$, representing the tangent line's slope at each curve point, exhibits an initial upward trend, a subsequent decrease, an upward trajectory, and ultimately a downward trend. In stage IV, the concrete on the outer arc is crushed. The concrete falls off severely, resulting in lower joint stiffness and a greater joint angle change than in the stage III. However, the changing trend is shorter because the joint has already started to break down and cannot bear the bending moment radically.

The inaccuracy in Figs. 20 and 21 mainly originate from stages II and IV. In stage II, the stress growth is accelerated due to the cracking of the concrete when the load reaches 64 kN, and the compression zone of the concrete on the joint surface gradually moves upward, and the bolt becomes the main bearing component. The bolts will be loosened in the experiment process, resulting in uneven forces and errors in the numerical simulation results. In stage IV, the overall structure had been seriously damaged, with spalling of the concrete on the outer arc and widening of the cracks on the inner arc,

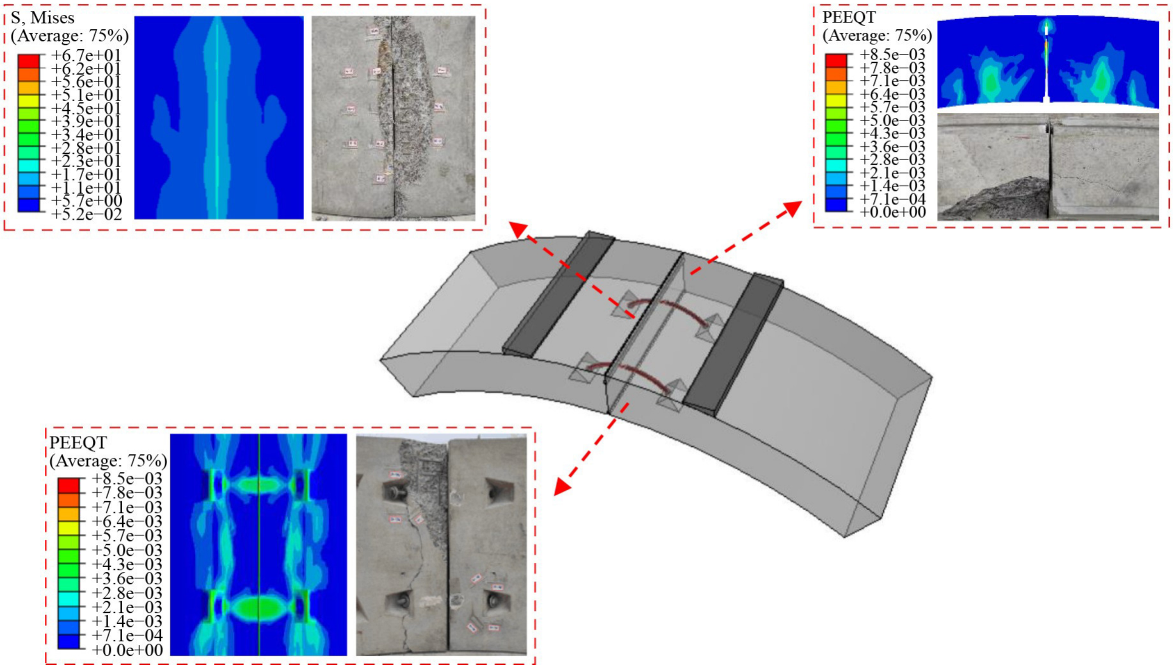

Fig. 19 Comparison of simulated and experimental final damage state.

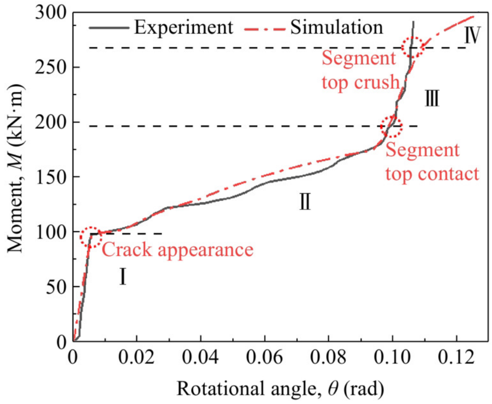

Fig. 20 Comparison of joint stiffness.

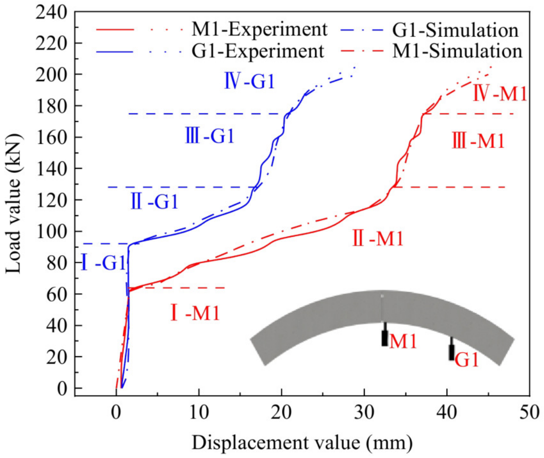

Fig. 21 Load–deflection comparison diagram.

which affected data collection. At the same time to ensure the safety of the experiment, with the severe damage form as the loading termination mark, there may be a certain deviation from the actual tunnel joint bearing performance of the shield segment joints in the stage of the ultimate damage state. Generally speaking, the numerical simulation and experimental fitting results are in perfect accordance with each other and can represent the damage characteristics of the shield joints.

3.3.2 Simulated characteristic load determination

According to the test results, the joint damage process was divided into four stages, and the initial load of each stage was defined as the characteristic load. Meanwhile, the characteristic load values were verified using numerical simulations.

1) Cracking load

In the test, the concrete at the location of the inner arc hand hole cracked, marking the model as entering the internal arc damage phase. This critical value is defined as the cracking load. The cracking characteristics can be determined from the concrete's equivalent plastic tensile strain values in numerical simulations. The model uses concrete with a strength class of C50 and an ultimate tensile strain value of 7.6×10^{-5}. Therefore, in the numerical simulation, an equivalent plastic strain greater than 7.6×10^{-5} indicates that the cracking load has been reached, as shown in Fig. 22.

2) Failure load

Figure 23(a) represents a fitted comparison between numerical simulations and experiments when the outer curved concrete is in contact, where the vertical coordinates represent the joint void spacing and the horizontal coordinates represent the load values. According to the specimen structure, the initial joint gap spacing of the 3D finite element numerical model was 4 mm. With the increase of load, the inner arc joint angle gradually increases, and the joint gap spacing is reduced, in the initial period due to the small load change. Therefore, the curve development trend is slow. As the load increases, the rate of change of the joint gap spacing with the load accelerates, and when the load reaches 128 kN, contact extrusion occurs on the outer arc, at which time the joint gap spacing is 0 mm. According to the images, it can be seen that the numerical simulation and experimental data fit well, and the numerical model calculation results can reflect the experimental phenomena well. In the experiment, the contact of concrete on the outer arc surface marked the entry of the model into the stage of the overall destruction of the joint, and this critical load was defined as the damage load. The numerical model, is shown in Fig. 23(a), and the cloud representation of hand hole crack development in the inner arc surface is shown in Fig. 23(b).

3) Ultimate load

In the test, the outer arc surface and side concrete appear to have large areas of falling blocks, indicating that the model has entered the joint limit damage stage. This critical load is defined as the ultimate load. In the numerical simulation, the concrete damage cloud through the outer arc surface, as well as the side, is shown in Fig. 24, indicating that the ultimate load (f_u) has been reached.

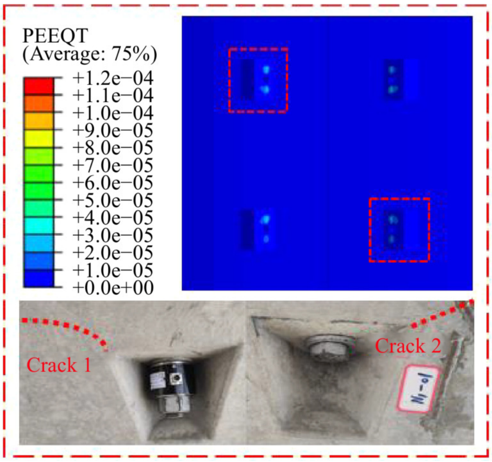

Fig. 22 Numerical simulation: cracking load characteristics.

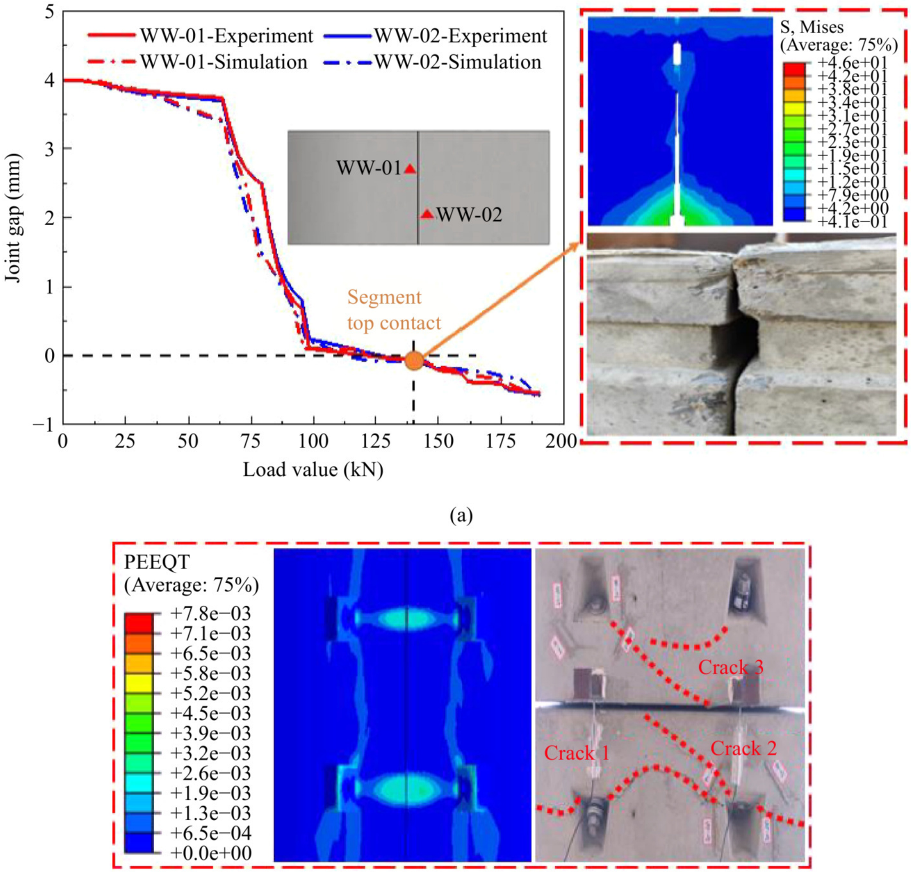

(a)

(b)

Fig. 23 Numerical simulation: failure load: (a) outer arc contact; (b) hand hole cracks.

By staging the experiment damage process, the damage characteristic load values of each stage were proposed. The corresponding results were extracted in numerical simulation and compared with the experiment. Some differences existed, caused by the difference between the location of the extracted point and the location of the experiment monitoring point, and the inaccuracy of the numerical simulation results and the experiment. Overall, the tolerance range of the characteristic load values in each stage is within 3%, which meets the tolerance requirement, and the numerical simulation can reflect the damage forms in each stage of the experiment. As shown in Table 2.

4 Parametric analysis

The existence of bolt hand holes in the inner arc will weaken the bending stiffness of the joint, and bolts connect the pipe segment. The lower part of the joint gradually opens with the increase in vertical load, and the concrete pressure zone will also move upward. Therefore, external load, concrete strength, and the performance of connecting bolts determine the joint's bearing capacity. This section focuses on the study of concrete strength, bolt strength, axial force, and bolt pre-stressing on the bearing performance of the joint part of the pipe segment, addressing the material properties and external structural loading. The base working conditions are variable, as shown in Table 3.

4.1 Material properties

4.1.1 Concrete strength

The grade of existing domestic segment concrete is basically between C30–C65. Due to the high cost of high-strength concrete and the stringent manufacturing process

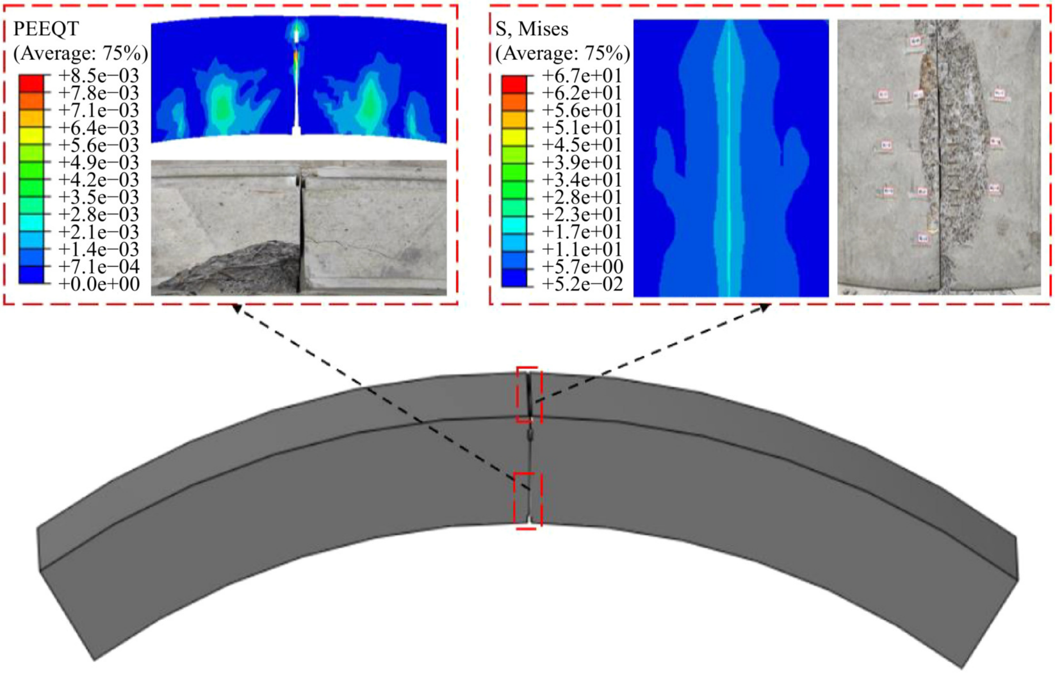

Fig. 24 Numerical simulation: ultimate load.

Table 2 Comparison of simulated-test characteristic load values

Stage	Characteristic load of the test (kN)	Characteristic load of the simulation (kN)	Tolerance (%)	Destruction deformation characteristics
I	–	–	–	No apparent cracks and joint deflection is unchanged.
II	64	66	3.1	Lateral concrete cracking, the sharp increase in joint deflection, and bolt tension.
III	128	130	1.6	Cracks in the inner arc are longitudinally penetrating, and concrete extrusion is in the outer arch.
IV	175	178	1.7	Side and outer curved concrete crushed off

Table 3 Variable reference base data table

Concrete strength	Elastic modulus of concrete (MPa)	Bolt strength class	Axial force (kN)	Bolt pre-stressing (kN)
C50	3.45×10^4	8.8	5	8

requirements, the application of concrete pipe pieces above C65 is extremely rare. To investigate the enhancement of concrete strength on the mechanical properties of joints, a controlled variable approach was used to vary only the concrete strength grade. At the same time, concrete grades C30, C40, C50, C60, and C65 were established for a total of 5 comparative working conditions to elucidate the impact of concrete strength on the load-bearing performance of joints.

To demonstrate more intuitively the effect of concrete strength on the mechanical properties of joints, the joint stiffness and rotation angle were defined using the names of each damage phase and were used to describe the changes in load-bearing properties for different concrete strength levels, as shown in Fig. 25.

Figure 25 shows that with the increase in concrete strength, the joint stiffness keeps increasing, and the joint rotation angle gradually decreases. The most significant difference in joint stiffness was produced by upgrading the concrete material from C50 to C60, with about 2.06, 3.29, and 0.67 times improvement in each stage. Additionally, due to the initial bolt pre-stressing and the small applied load, the change in cracking angle at each concrete strength is not apparent. Nevertheless, the ultimate angle decreases more noticeably when the concrete material is C40 or C60. The difference between the ultimate corner values of C65 and C60 concrete material is slight, indicating that C60 concrete can sufficiently enhance the overall joint stiffness.

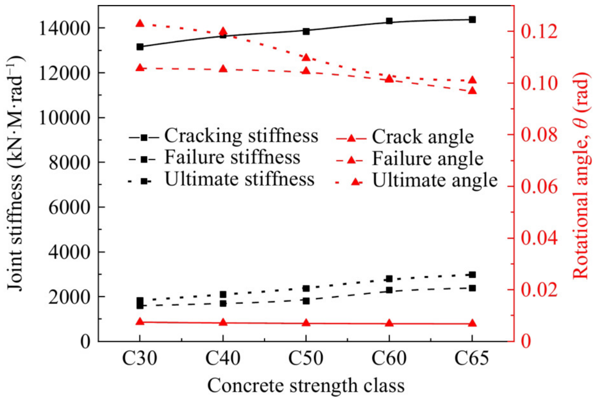

Fig. 25 Concrete strength–joint stiffness–rotation angle diagram.

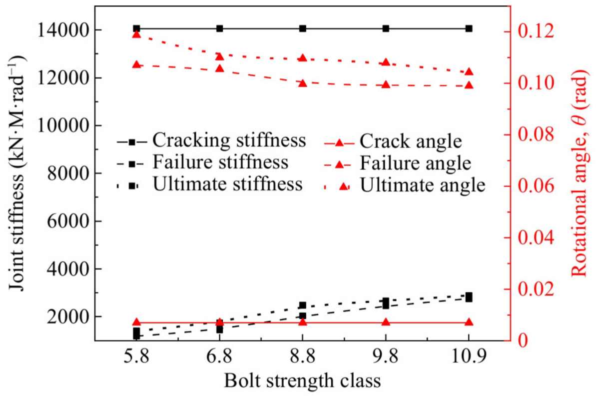

Fig. 26 Bolt strength–joint stiffness–rotation angle diagram.

4.1.2 Bolt strength

The bolt is the connecting part of the tube segment, and the strength of the bolt has a significant impact on the mechanical properties of the joint when loaded. Therefore, the bolt strength directly determines the bearing performance of the joint. Five sets of calculated working conditions were selected to systematically study the influence of the bolt strength on the mechanical properties: 5.8, 6.8, 8.8, 9.8, and 10.9.

To more intuitively demonstrate the effect of bolt strength on the mechanical properties of the joint, joint stiffness and rotation angle were used to describe the changes in load-bearing properties under different bolt grades. The results are shown in Fig. 26.

From Fig. 26, it can be obtained that the joint failure stiffness and ultimate stiffness increase as the bolt grade increases, and the joint failure and ultimate angle of rotation gradually decrease. Since the cracking stiffness of the joint depends mainly on the tensile properties of the concrete material, the cracking stiffness and the rotation angle of the cracked joint remain the same if only the strength of the bolts is changed. At the same time, the difference between the damage stiffness and the ultimate stiffness is significant, 40.1% and 42.2%, respectively, when the bolt grade is increased from 6.8 to 8.8, and the difference between the failure and ultimate stiffness of the joint decreases with the increase of the bolt grade, which indicates that there is an optimal fit between the bolt and the concrete so that the bolt can play a more significant role.

4.2 External loading

4.2.1 Axial force

To enhance the rigidity of joints and decelerate the formation of their rotational angles, the impact of axial force on the joint's mechanical characteristics is typically examined by exerting axial force at each end of the sample. Therefore, the axial force applied by changing the base working condition increases by 60% each time, and a total of 5 sets of axial forces are set to 5, 8, 13, 20, and 33 kN to analyze the influence of axial force on the structure.

To demonstrate the effect of the axial force on the joint, the variation of the axial force was analyzed using the characteristic load values for each stage as well as the joint stiffness and rotation angle, as shown in Figs. 27 and 28.

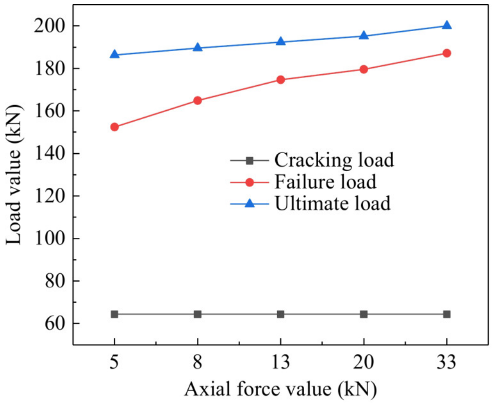

Fig. 27 Axial force–characteristic load diagram.

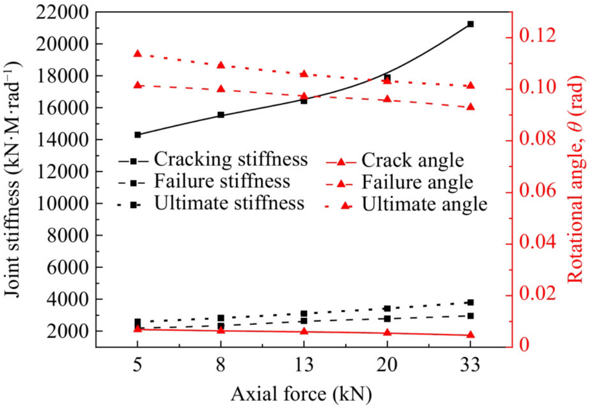

Fig. 28 Axial force–joint stiffness–rotation angle diagram.

It is evident from Fig. 27 that the damage load and ultimate load increase with the increasing axial force, but the cracking load is the same because the concrete material does not change. In addition, the difference between the ultimate load and the failure load values decreases as the axial force increases. The axial force reaches 33 kN, and the failure load is about 93.5% of the ultimate load, indicating that with the elevation of the axial force, the contact time of the outer arc concrete is delayed, and the more load it bears, the faster the failure occurs after contact.

As shown in Fig. 28, joint stiffness gradually increases with the continuous increase of the axial force, and the joint rotation angle tends to decrease. Although the concrete grade did not change, the cracking angle and stiffness changed. The cracking stiffness changed significantly with the increase in axial force because the axial force can make the tube segments fit better at the early loading stage, reduce the joint rotation angle, and offset part of the bending moment generated by the vertical load. Therefore, the axial force affects the cracking angle and stiffness. Meanwhile, the difference between failure and ultimate stiffness increases with the increase of axial force, with a maximum difference of 11.35%. In contrast, the difference between failure and the ultimate angle of rotation decreases with the growth of axial force, with a minimum difference of 0.0069 rad, indicating that the improvement of axial force has a more significant influence on the stiffness of the joint.

4.2.2 Bolt pre-stressing

During the assembly stage of the test, stress is generated when tightening the bolts to secure them and prevent them from falling off during the loading process. This prestressing also allows for a better fit of the tube sheet before loading, reducing the rotation angle of the joint during the loading stage. To study the effect of prestressing on the mechanical properties of the joint, increase the value of prestressing in the basic parameters. At the same time, ensure that the maximum stress produced by prestressing the concrete in the handhole area is not greater than 80% of the compressive strength of concrete. Set up five groups of bolts with prestressing of 8, 28, 48, 68, 88 kN in increments of 20 kN to calculate the conditions and analyze the prestressing effect on the structure.

To more intuitively demonstrate the change in the influence of pre-stressing on the structure, the analysis of each set of conditions is conducted through characteristic load, joint stiffness, and rotation angle in each stage. This is illustrated in Figs. 29 and 30.

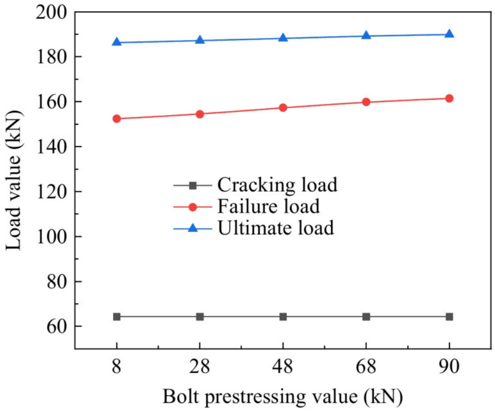

Fig. 29 Bolt pre-stressing–characteristic load diagram.

From Fig. 29, it can be seen that increasing the bolt pre-stress has no pronounced effect on the concrete cracking load, verifying that the appearance of cracks in the concrete signifies the end of the elastic stage. As the bolt pre-stressing force continues to increase, the failure load and ultimate load of the joint show a gradual increase. This is because the bolt pre-stressing force improves the contact between tube segments at the initial stage, requiring a higher load value for the same rotation angle. This indicates that the bolt pre-stressing force is beneficial for improving the bearing performance of the joint.

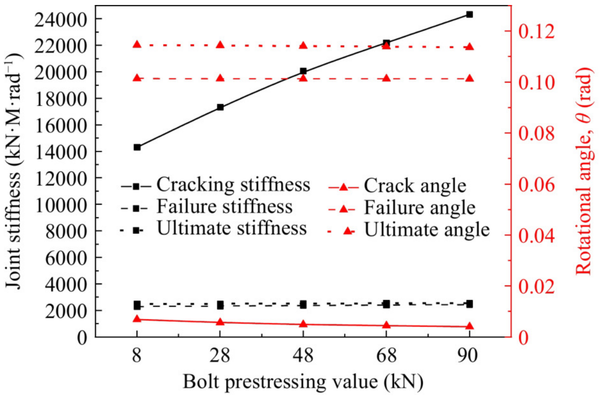

Fig. 30 Bolt prestressing–joint stiffness–rotation angle diagram.

According to the calculation results, the variation of the effect of prestressing on the joint stiffness was analyzed, as shown in Fig. 30. From the figure, it can be seen that the joint stiffness gradually increases, and the rotation angle gradually decreases with the increase of bolt pre-stress. Because the bolt pre-stress is applied before loading, and as the load increases, the connection between the bolt and the tube fragment will loosen, causing the pre-stress to gradually decrease. Therefore, the cracking stiffness and rotation angle change more noticeably with the bolt pre-stress, while the rest of the variables show no significant change.

5 Discussion

5.1 Concrete and bolt grade fitment

In the actual construction process, due to the difficulty and high cost of producing excessively high-strength concrete, choosing the proper concrete strength can improve performance while increasing the economic benefits of construction. The grade of the bolts should also match the concrete's strength so that each component's performance can be enhanced. In combination with the previous analysis, studying the concrete and bolt adaptation in depth and using the right combination of materials can improve each component's performance. Meanwhile, using the control variables method, each concrete strength grade in the C30–C65 range and each bolt strength grade in the 5.8–10.9 range were calculated for 25 sets of conditions.

According to the four-stage characteristics of joint damage, it can be seen that at the end of the stage, the crack at the handhole determines the failure, and the cracking load value is consistent because the tensile properties of each grade of concrete lifting are not prominent. After stage III, the external load increases because of the outer arc's concrete contact. Combined with the force change law of the bolts in Fig. 6, it can be obtained that the bolts mainly play a more prominent role during stage II. The specific calculation results of each parameter are as follows.

Figure 31(a) reflects the effect of concrete strength on the characteristic load values at each stage for different strength bolts. The vertical coordinate represents the characteristic load difference between adjacent damage stages, which illustrates the degree of contribution of different concrete strengths to the characteristic loads of shield segment joints under the same bolt grade. The horizontal coordinate represents the bolt strength grade, and each curve indicates the size of the difference in the characteristic load of the adjacent damage stage under the same concrete strength grade and different bolt strength grades, and the larger the difference is, the better the fitness of the concrete strength grade and the bolt strength grade. It is obtained in Fig. 31(a) that the difference increases continuously with the increase of concrete and bolt strength class, and the most significant variation of the difference is observed when the bolt class is increased

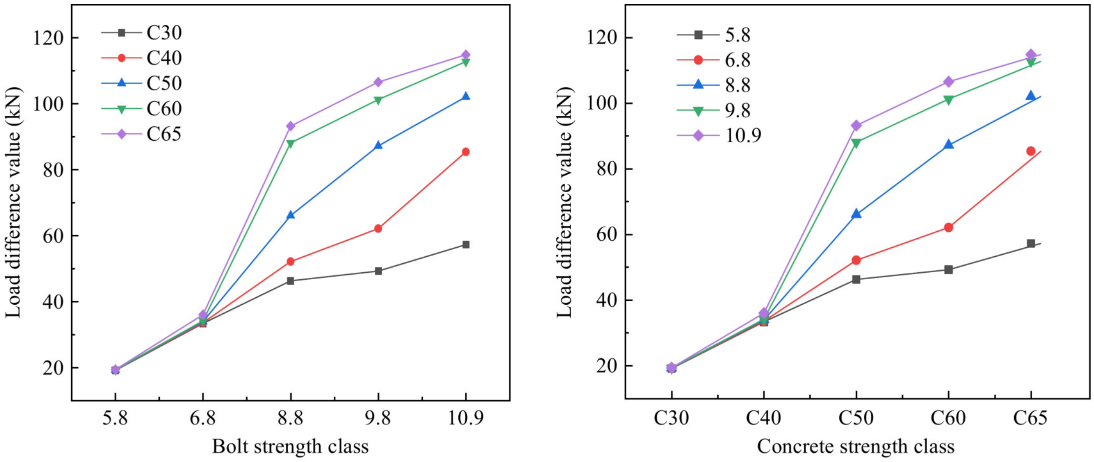

(a) (b)

Fig. 31 Bolt and concrete diagrams for each grade: (a) bolt-concrete grade diagram; (b) concrete-bolts grade diagram.

from 6.8 to 8.8. Figure 31(b) reflects the effect of bolt strength on the values of characteristic loads at various stages for different concrete strength classes. The vertical coordinate represents the characteristic load difference between adjacent damage stages, which illustrates the contribution of different bolt strengths to the characteristic loads of shield segment joints under the same concrete strength by the characteristic load difference. The horizontal coordinate represents the concrete strength grade, and each curve indicates the size of the difference between the characteristic loads of adjacent damage stages at different concrete strength grades under the same bolt strength, and the larger the difference, the better the fitness of the concrete strength grade and the bolt strength grade. From Fig. 31(b), it can be seen that when the bolt grade is raised from 6.8 to 8.8, the difference is about 53.95 kN. Although the corresponding value for C65 concrete is larger, the difference is only 11.37% smaller compared to that for C60 concrete with the strength of C65 concrete and the difference is nearly raised by a factor of 3.7 in comparison to that for C50 concrete with the strength of C60 concrete.

5.2 Axial force and bolt pre-stress contribution

During construction, pre-stress is applied to the bolts to ensure a better connection between the bolts and the segments. To study the effect of axial force and bolt pre-stress on joint performance, the initial axial force of 5 kN and bolt pre-stress of 8.2 kN were used as the base variables. According to the optimal concrete and bolt strength grades discussed in Subsection 6.1, the parameters were used to increase the two variables of axial force and bolt pre-stress by 20%, 40%, 60%, and 80% simultaneously, and eight groups of comparison data were set, as shown in Table 4.

To demonstrate more clearly the effects produced by axial forces and bolt pre-stressing, the characteristic loads of each damage stage are cited for description, as shown in Fig. 32.

The percentage increase in Fig. 32 is based on an axial force of 5 kN and a bolt pre-stress of 8.2 kN. The figure shows that both can increase the failure load and the ultimate load, and the axial force has a more significant effect on the failure load and the ultimate load than the bolt pre-stressing. At the same time, the characteristic load value increased by each level of bolt pre-stressing is very small, so in the construction process, the minimum required value of the bolt pre-stressing can be considered based on economic efficiency and ease of application. Concurrently, the typical load value escalates with every stage of bolt prestressing, remaining minimal. Consequently, during construction, the least necessary amount of bolt pre-stressing should be evaluated due to its cost-effectiveness and simplicity of use.

Table 4 Calculation parameters

Added value	Axial force (kN)	Bolt pre-stressing (kN)
20%	6	8.2
	5	9.84
40%	7	8.2
	5	11.48
60%	8	8.2
	5	13.12
80%	9	8.2
	5	14.76

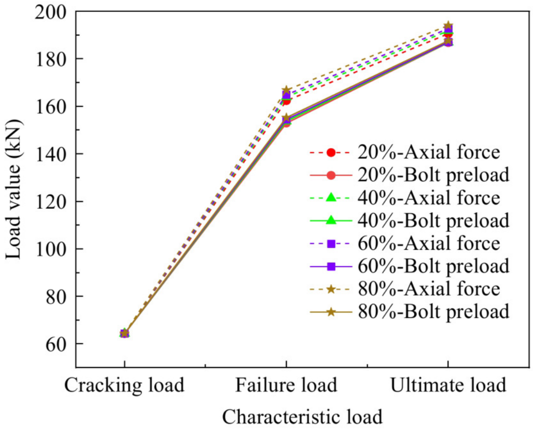

Fig. 32 Axial force and bolt pre-stressing–characteristic load diagram.

6 Conclusions

This article investigates the mechanical characteristics of joints with curved bolts in shield lining by combining full-scale experiments and numerical simulation. The damage law of tunnel joints and the development law of concrete strain in each part of tunnel joints are analyzed. Moreover, considering the material properties and external load, the parametric analysis came up with the influence of concrete strength, bolt strength, axial force, bolt preload and other factors on the mechanical properties of tunnel joints. The main conclusions are as follows.

1) The damage process of shield joints with curved bolt connections can be divided into four stages: concrete elasticity (stage I), concrete cracking (stage II), overall joint damage (stage III), and ultimate joint damage (stage IV). The initial loads of the adjacent damage stages are defined as the characteristic loads of cracking, the damage and the ultimate load.

2) The bearing performance of the shield joint weakens after the concrete cracking while enhanced after the contact of concrete on the outer arc surface. Improving the strength of concrete and bolts has a pronounced effect

on the bearing performance of the joint, which strengthens the mechanical bearing performance of each component itself, thus greatly helping the stiffness and bearing capacity of the joint. At the same time, in the bearing process, the pressure zone of the concrete in the joint area shifted upward with the increasing tension angle of the inner arc surface, the bolt became the main bearing component in stage II, and the stress growth rate was accelerated, and after the concrete contact of the outer arc surface, the concrete became the main bearing component again.

3) The concrete strength has a more significant influence on the mechanical properties of the shield joints than the bolt strength, while the rest of the parameters remain constant. The C60 concrete and the 8.8-grade bolts are the optimal combination to enhance the load-bearing performance of shield joints, which can maximize the mechanical load-bearing performance of shield joints.

4) When the difference between the axial force and the bolt preload is less than 3 times, the enhancement effect of the axial force on the shield joint is more obvious, and the higher the axial force, the greater the enhancement effect on the stiffness of the shield joint. At the same time, when both values are less than one loaded tenth, the axial force and bolt preload have essentially the same effect on shield joint lifting.

5) The article thoroughly investigated the mechanical properties of segment joints connected by curved bolts. However, there are still some lacks, such as neglecting shield joints with inclined bolts and straight bolts, and further comparing the three types of traditional bolts. On the other hand, the bearing situation of the joints among the whole ring lining remains exploration. Future research is expected to deepen the aforementioned directions.

Acknowledgements The authors gratefully acknowledge the financial support provided by the National Natural Science Foundation of China under (Grant Nos. 51978019 and 52278382) and the Natural Science Foundation of Beijing Municipality (No. 8222004).

Competing interests The authors declare that they have no competing interests.

References

1. Lou P, Li Y, Lu S, Xiao H, Zhang Z. Deformation and mechanical characteristics of existing foundation pit and tunnel itself caused by shield tunnel undercrossing. Symmetry, 2022, 14(2): 263
2. Li X, Li X K. A soil freezing–thawing model based on thermodynamics. Cold Regions Science and Technology, 2023, 211: 103867
3. Li X, Li X, Liu J. A dynamic soil freezing characteristic curve model for frozen soil. Journal of Rock Mechanics and Geotechnical Engineering, 2024, 16(8): 3339–3352
4. Fahiminia M, Shishegaran A. Evaluation of a developed bypass viscous damper performance. Frontiers of Structural and Civil Engineering, 2020, 14(3): 773–791
5. Molins C, Arnau O. Experimental and analytical study of the structural response of segmental tunnel linings based on an *in situ* loading test. Part 1: Test configuration and execution. Tunnelling and Underground Space Technology, 2011, 26(6): 764–777
6. Liu X, Dong Z, Bai Y, Zhu Y. Investigation of the structural effect induced by stagger joints in segmental tunnel linings: First results from full-scale ring tests. Tunnelling and Underground Space Technology, 2017, 66: 1–18
7. Lee W F, Ishihara K. Forensic diagnosis of a shield tunnel failure. Engineering Structures, 2010, 32(7): 1830–1837
8. Wang S C, Jiang X, Bai Y. The influence of hand hole on the ultimate strength and crack pattern of shield tunnel segment joints by scaled model test. Frontiers of Structural and Civil Engineering, 2019, 13(5): 1200–1213
9. Zhang J, Zhao M. Design and Research of the Bending Test Set-up for the Longitudinal Joints in Segmental Tunnel Linings. IOP Conference Series: Materials Science and Engineering. IOP Publishing, 2019, 603(5): 052017
10. Gong C J, Ding W, Soga K, Mosalam K M, Tuo Y. Sealant behavior of gasketed segmental joints in shield tunnels: An experimental and numerical study. Tunnelling and Underground Space Technology, 2018, 77: 127–141
11. Zhang J W, Guo S C, Chen Y Y. Mechanical behavior of sealed waterproof for shield tunnel segment joint under different assembling ellipticity. Science Progress, 2021, 104(1): 54–68
12. Wang J, Liu H Q, Liu H B. Measuring joint opening displacement between model shield-tunnel segments for reduced-scale model tests. Structures, 2018, 16: 112–118
13. Tan X Y, Chen W, Wu G, Wang L, Yang J. A structural health monitoring system for data analysis of segment joint opening in an underwater shield tunnel. Structural Health Monitoring, 2020, 19(4): 1032–1050
14. Ding W Q, Peng Y C, Yan Z G, Shen B W, Zhu H H, Wei X X. Full-scale testing and modeling of the mechanical behavior of shield TBM tunnel joints. Structural Engineering and Mechanics, 2013, 45(3): 337–354
15. Jusoh S N, Mohamad H, Marto A, Kassim F. Assessment on segment joint to improve soil-tunnel interaction. In: Proceedings of 12th International Civil Engineering Post Graduate Conference (SEPKA)/3rd International Symposium on Expertise of Engineering Design (ISEED). Paris: EDP Sciences, 2018
16. Liu F J, Fang A L. Study on Test Scheme of Shield Tunnel Prestressed Segment Joint. In: Proceedings of 2nd International Conference on Civil Engineering, Architecture and Sustainable Infrastructure (ICCEASI 2013). Lausanne: Trans Tech Publications, 2013
17. Shi C H, Cao C, Lei M, Yang W. Sealant performance test and stress-seepage coupling model for tunnel segment joints. Arabian Journal for Science and Engineering, 2019, 44(5): 4201–4212
18. Zhang W J, Qi J, Zhang G, Niu R, Zhang C, He L, Lyu J. Full-scale experimental study on failure characteristics of the key segment in shield tunnel with super-large cross-section. Tunnelling and Underground Space Technology, 2022, 129: 104671
19. Zuo L B, Li G, Feng K, Ma X, Zhang L, Qiu Y, Cao S, Feng L.

Experimental analysis of mechanical behavior of segmental joint for gas pipeline shield tunnel under unfavorable compression-bending loads. Tunnelling and Underground Space Technology, 2018, 77: 227–236

20. Wang F Y, Huang H, Zhang D, Zhou M. Cracking feature and mechanical behavior of shield tunnel lining simulated by a phase-field modeling method based on spectral decomposition. Tunnelling and Underground Space Technology, 2022, 119: 104246
21. Liu X, Zhang Y M, Bao Y H. Full-scale experimental investigation on stagger effect of segmental tunnel linings. Tunnelling and Underground Space Technology, 2020, 102: 103423
22. Wang Q, Geng P, Guo X, Zeng G, Chen C, He C. Experimental study on the tensile performance of circumferential joint in shield tunnel. Tunnelling and Underground Space Technology, 2021, 112: 103937
23. Zhang Y J, Huang H, Zhang D, Ayyub B M. Deformation recoverability of longitudinal joints in segmental tunnel linings: An experimental study. Tunnelling and Underground Space Technology, 2022, 124: 104475
24. Liu J W, Shi C, Lei M, Cao C, Lin Y. Improved analytical method for evaluating the responses of a shield tunnel to adjacent excavations and its application. Tunnelling and Underground Space Technology, 2020, 98: 103339
25. Shi C H, Cao C, Lei M, Peng L, Ai H. Effects of lateral unloading on the mechanical and deformation performance of shield tunnel segment joints. Tunnelling and Underground Space Technology, 2016, 51: 175–188
26. Chen R P, Meng F, Ye Y, Liu Y. Numerical simulation of the uplift behavior of shield tunnel during construction stage. Soil and Foundation, 2018, 58(2): 370–381
27. Karami B, Shishegaran A, Taghavizade H, Rabczuk T. Presenting innovative ensemble model for prediction of the load carrying capacity of composite castellated steel beam under fire. Structures, 2021, 33: 4031–4052
28. Shishegaran A, Karami B, Rabczuk T, Shishegaran A, Naghsh M A, Mohammad Khani M. Performance of fixed beam without interacting bars. Frontiers of Structural and Civil Engineering, 2020, 14(5): 1180–1195
29. Shishegaran A, Khalili M R, Karami B, Rabczuk T, Shishegaran A. Computational predictions for estimating the maximum deflection of reinforced concrete panels subjected to the blast load. International Journal of Impact Engineering, 2020, 139: 103527
30. Bigdeli A, Shishegaran A, Naghsh M A, Karami B, Shishegaran A, Alizadeh G. Surrogate models for the prediction of damage in reinforced concrete tunnels under internal water pressure. Journal of Zhejiang University. Science A, 2021, 22(8): 632–656
31. Zhao T S, Liu W, Ye Z. Effects of water inrush from tunnel excavation face on the deformation and mechanical performance of shield tunnel segment joints. Advances in Civil Engineering, 2017, 2017: 5913640
32. Tsiampousi A, Yu J, Standing J, Vollum R, Potts D. Behaviour of bolted cast iron joints. Tunnelling and Underground Space Technology, 2017, 68: 113–129
33. Shishegaran A, Moradi M, Naghsh M A, Karami B, Shishegaran A. Prediction of the load-carrying capacity of reinforced concrete connections under post-earthquake fire. Journal of Zhejiang University. Science A, 2021, 22(6): 441–466
34. Naghsh M A, Shishegaran A, Karami B, Rabczuk T, Shishegaran A, Taghavizadeh H, Moradi M. An innovative model for predicting the displacement and rotation of column-tree moment connection under fire. Frontiers of Structural and Civil Engineering, 2021, 15(1): 194–212
35. Kou L, Xiong Z, Cui H, Zhao J. Study on mechanical characteristics of segmental joints of a large-diameter shield tunnel under ultrahigh water pressure. Sensors, 2021, 21(24): 8392
36. Dong L W, Yang Z Y, Wang Z Y, Ding Y W, Qi W Q. Study on Internal Force of Tunnel Segment by Considering the Influence of Joints. Advances in Materials Science and Engineering, 2020, 2020: 1020732
37. Li B Q, Zhang Z, Wang X, Liu X. Investigation on cohesive zone model of bolted joint for water conveyance tunnel lining. Engineering Computations, 2019, 36(5): 1449–1468
38. Zheng G, Cui T, Cheng X, Diao Y, Zhang T, Sun J, Ge L. Study of the collapse mechanism of shield tunnels due to the failure of segments in sandy ground. Engineering Failure Analysis, 2017, 79: 464–490
39. Liu J W, Shi C, Wang Z, Lei M, Zhao D, Cao C. Damage mechanism modelling of shield tunnel with longitudinal differential deformation based on elastoplastic damage model. Tunnelling and Underground Space Technology, 2021, 113: 103952
40. Kakavand M R A, Taciroglu E. An enhanced damage plasticity model for predicting the cyclic behavior of plain concrete under multiaxial loading conditions. Frontiers of Structural and Civil Engineering, 2020, 14(6): 1531–1544
41. Shishegaran A, Varaee H, Rabczuk T, Shishegaran G. High correlated variables creator machine: Prediction of the compressive strength of concrete. Computers & Structures, 2021, 247: 106479
42. Wei G, Wang Q, Zhou X, Feng F, Wang X, Zhang L, Liang L. Experiments and numerical simulation of the reinforcement effect of channel-steel-reinforced shield tunnel segments under unloading conditions. European Journal of Environmental and Civil Engineering, 2023, 27(14): 4142–4164
43. Wang J, Liu H B. Transverse seismic responses of a shield tunnel considering the influence of segment joints. Tunnelling and Underground Space Technology, 2023, 142: 105423
44. Wu Z W, Zhang C, Mou L, Mei G, Garg A. Dynamic performance of submerged floating tunnel with different mooring styles subjected to anchor cable failure. Frontiers of Structural and Civil Engineering, 2023, 17(10): 1443–1464
45. Li H Y, Li X G, Liu H. Deformation and failure mechanism of metro shield tunnel subjected to buried fault dislocation. Engineering Failure Analysis, 2023, 153: 107551
46. Chung W C, Jin C, Kim M, Hwang J Y. Comparison study and forensic analysis between experiment and coupled dynamics simulation for submerged floating tunnel segment with free ends under wave excitations. Computer Modeling in Engineering & Sciences, 2023, 137(1): 155–174